Super-resolved Multi-channel Fuzzy Segmentation of MR Brain Images

Ying Bai[a], Xiao Han[a], Dzung L. Pham[b], and Jerry L. Prince[a]

[a] Image Analysis and Communication Laboratory, Johns Hopkins University,Baltimore MD 21218 [b] Laboratory of Medical Image Computing, Johns Hopkins University, Baltimore MD 21287

ABSTRACT

We propose a new fuzzy segmentation framework that incorporates the idea of super-resolution image reconstruction. The new framework is designed to segment data sets comprised of orthogonally acquired magnetic resonance (MR) images by taking into account their different system point spread functions. Formulating the reconstruction within the segmentation framework improves its robustness and stability, and makes it possible to incorporate multispectral scans that possess different contrast properties into the super-resolution reconstruction process. Our method has been tested on both simulated and real 3D MR brain data.

Keywords: Fuzzy segmentation, super-resolution image reconstruction, brain cortex segmentation, MRI

1. INTRODUCTION

Segmentation of brain structures is often the first step in quantitative magnetic resnaonce (MR) imaging-based neuroscience studies. Segmentation accuracy, however, is inherently limited by the resolution of the acquired images. Due to hardware limitations and imaging time considerations, a typical 3D multislice MR scan often has poorer resolution in the slice-selection direction than in the in-plane directions. For example, in the Baltimore Longitudinal Study on Aging (BLSA) neuroimaging project,[1] two T1-weighted scans are acquired in approximately orthogonal orientations, each with non-isotropic voxels (both 0.9375 mm by 0.9375 mm in-plane and 1.5 – 1.6 mm out of plane).

One of the goals of our group has been the segmentation and reconstruction of the cerebral cortex. We have developed an automatic processing "pipeline" for cortical surface reconstruction from 3D MR brain images.[2] Currently, our methods are optimized for the processing of a single input image (the axial scan from the BLSA database). Because the accuracy of the surface reconstruction is limited by the resolution of the source image data, the relatively large slice thickness of the axial scan can yield poor results at some locations in the brain. In particular, this can occur when attempting to delineate the pial surface or estimate cortical thickness within tightly folded sulcal regions that are orthogonal to the acquisition plane. It is conceivable that by making use of the two scans that contain complementary spatial resolutions, we can improve the segmentation result and thus achieve a more accurate and more reliable cortical reconstruction.

In a previous attempt to combine these two low-resolution scans,[3] we followed the general approach of super-resolution image reconstruction, and adopted a maximum a posteriori (MAP) super-resolution framework

Further author information: (Send correspondence to Jerry L. Prince)
E-mail: prince@jhu.edu, Telephone: 1 410 516 5192

Medical Imaging 2005: Image Processing, edited by J. Michael Fitzpatrick, Joseph M. Reinhardt, Proc. of SPIE Vol. 5747 (SPIE, Bellingham, WA, 2005)
1605-7422/05/$15 · doi: 10.1117/12.595357

to reconstruct a single isotropically high-resolution image from two orthogonal lower-resolution scans. One difficulty we observed is that the super-resolution reconstruction is a highly unstable processs, and a strong image prior has to be imposed to ensure computational stability. However, the image prior (usually a smoothness constraint) often limits the resulting resolution improvement.

In this work, we propose to incorporate the idea of super-resolution directly into a fuzzy segmentation framework. The integration of these two steps reduces the overall computation time, and addresses the instability of the inverse reconstruction problem. Also this new framework makes it possible to incorporate multispectral (eg. T2- and PD-weighted) scans into the super-resolution reconstruction process.

Several methods for reconstruction of an isotropic high resolution image from several lower resolution MR scans can be found in the literature.[4,5] These methods typically assume an over-simplified model of the MR imaging process, and the reconstruction methods are sub-optimal. In another closely related work,[6] an efficient edge-preserving regularized reconstruction method is proposed for recovering a high-resolution image from several low-resolution acquisitions. The imaging method used to acquire the low-resolution data in this approach is different from the method we used, which results in a different problem formulation. In addition, their method can not be directly applied to combine multi-channel or multispectral data into the image reconstruction algorithm due to their different contrast properties.

The rest of the paper is organized as follows. In Section 2, we introduce our new method and describe the steps of the new segmentation algorithm. In Section 3, we show results of several experiments using both simulated and real data sets. In Section 4, we conclude with some directions for future investigation.

2. METHODS

The method we propose in this work builds upon our previously developed Fuzzy And Noise Tolerant Adaptive Segmentation Method (FANTASM).[7] By incorporating the different system point spread function (PSF) for each individual image channel into FANTASM, the new method simultaneously performs both image segmentation and image resolution restoration. In the following, we first revisit the FANTASM algorithm, and then we introduce the new algorithm which combines FANTASM with image restoration.

2.1. The FANTASM algorithm

FANTASM is derived from the fuzzy c-means clustering algorithm. It automatically produces a soft or fuzzy image segmentation while simultaneously adapting to the intensity inhomogeneity artifact in the input image. It also introduces a spatial smoothness constraint in order to reduce the effect of image noise. We briefly describe the algorithm here.

FANTASM is formulated as the minimization of the following objective function with respect to the membership function u, the centroids $\mathbf{v}$ and the scalar gain field g:

$$J = \sum_{j\in\Omega}\sum_{k=1}^{K} u_{jk}^{q}||\mathbf{y}_j - g_j\mathbf{v}_k||^2 + \frac{\beta}{2}\sum_{j\in\Omega}\sum_{k=1}^{K} u_{jk}^{q}\sum_{l\in N_j}\sum_{m\in M_k} u_{lm}^{q} + \lambda_1\sum_{j\in\Omega}\sum_{r=1}^{R}(D_r * g)_j^2 + \lambda_2\sum_{j\in\Omega}\sum_{r=1}^{R}\sum_{s=1}^{R}(D_r * D_s * g)_j^2 \quad (1)$$

Here Ω is the set of voxel indices in the image domain, u_{jk} is the membership value at voxel location j for class k such that $\sum_k^K u_{jk} = 1$, $\mathbf{y}_j$ be the observed (vector) intensity value at location j, $\mathbf{v}_k$ is the centroid of class k, g_j is the scalar gain field. The total number of classes K is assumed to be known. The parameter q, which must satisfy $q > 1$ (and is set to 2 in this work), determines the amount of "fuzziness" of the resulting classification. The norm operator $||\cdot||$ is assumed to be the standard Euclidean distance. The parameters β, λ_1, and λ_2 are weights that control the amount of smoothness in resulting membership functions (β) and the gain field (λ_1 and λ_2), and are empirically determined. The symbol N_j represents the set of first order neighbors of pixel j. The expressions $D_r * g$ and $D_r * D_s * g$ represent first- and second-order finite differences applied to the gain field (details on this notation can be found in [8]).

In the objective function (1), the first term is minimized when high membership values are assigned to voxels whose intensities are close to the centroid for its particular class and low membership values are assigned when the voxel intensity is far from the centroid. The second penalty term forces the membership values at each voxel to be dependent on its neighbors. It is minimized when the membership value for a particular class is large and the membership values for the other classes at neighboring voxels are small (and vice versa). The last two terms are first- and second-order regularization terms used to ensure that g_j is spatially smooth and slowly varying.

The minimization of this objective function can be achieved by taking the first derivatives of J with respect to each unknown variable, setting them to zero, and iterating through these three necessary conditions for J to be at a minimum. The detailed algorithm has been previously reported.[7]

Finally, the resulting fuzzy segmentation (i.e. the membership functions u) can be converted to a hard or crisp segmentation by assigning each pixel solely to the class that has the highest membership value for that pixel. This is known as a maximum membership segmentation (or hard segmentation).

2.2. The proposed method

It is clear that we can directly apply FANTASM on two orthogonal scans of the same subject by considering them as two components of a multi-spectral image. This formulation, however, ignores the anisotropic resolution of the two scans. Since the PSF of an MRI scanner can be assumed to be known, by combining the two images through a superresolution-like image restoration procedure, the resolution and accuracy of the final segmentation can be improved.

We formulate the super-resolution restoration in the space of membership functions. The objective is to directly obtain a high-resolution fuzzy segmentation from multiple low resolution images. Since the fuzzy membership functions describe the spatial distribution of different tissue classes, we can assume that the system PSF is also a good model of the blurring of the high-resolution membership functions to the space of the low-resolution images. With this consideration, we arrive at a modified objective function as shown in Eq.(2), where we adopt the matrix notation as commonly used in the super-resolution literature:

$$J_{\text{new}} = \sum_{m=1}^{M} \left(\frac{1}{\sigma_m^2} \sum_{k=1}^{K} (\mathbf{H}_m \mathbf{u}_k)^T \mathbf{B}_{mk} (\mathbf{H}_m \mathbf{u}_k) \right) + \frac{\beta}{2} \sum_{k}^{K} \mathbf{u}_k^T \mathbf{R}_k \mathbf{u}_k + \lambda_1 ||\mathbf{D}_r \mathbf{g}||^2 + \lambda_2 ||\mathbf{D}_r \mathbf{D}_s \mathbf{g}||^2 \tag{2}$$

In Eq.(2), we have assumed the fuzziness parameter q is 2. The difference of Eq.(2) and Eq.(1) only lies in the first term. (i.e. the remaining terms are simply the matrix form of the corresponding terms in Eq.(1).) In the first term of Eq.(2), M denotes the total number of low resolution scans, and σ_m, which can be estimated beforehand,[9] is the standard deviation of image noise in the m-th input image. Adding this weight ensures that the input data with higher signal-to-noise ratio is given more priority. $\mathbf{B}_{mk}$ for each m and k is a diagonal matrix with the j-th diagonal term equal to $||y_{mj} - g_j v_{mk}||^2$. $\mathbf{H}_m$ is the blurring matrix associated with the m'th channel PSF. In this particular problem, the PSF for each channel is approximated as a truncated Gaussian kernel in the slice-selection direction, with the FWHM set to be the slice thickness.

We follow the minimization procedure in Section 2.1 by solving for the zero gradient condition with respect to each unknown variable and iterating through each of these necessary conditions for J_{new} to be at a minimum. This yields the following algorithm for super-resolved fuzzy segmentation (the equations for which are derived in Appendix A):

1. Obtain an initial estimate of the centroids $\mathbf{v}_k$ (using the method as in [8]).

2. Compute the membership functions by Eq.(3):

$$u_{jk} = \frac{\frac{1}{\sum_k \frac{1}{\mathbf{C}_{k(jj)}+\beta \mathbf{R}_{k(jj)}}} \left(1 + \sum_k \left(\frac{\sum_{i \neq j} \mathbf{C}_{k(ji)} \mathbf{u}_{k(i)}}{\mathbf{C}_{k(jj)} + \beta \mathbf{R}_{k(jj)}} \right) \right) - \sum_{i \neq j} \mathbf{C}_{k(ji)} \mathbf{u}_{k(i)}}{\mathbf{C}_{k(jj)} + \beta \mathbf{R}_{k(jj)}} \tag{3}$$

   for all $j \in \Omega$ and $k = 1, ..., K$, where

$$\mathbf{C}_k = \sum_m \mathbf{H}_m^T \mathbf{B}_{mk} \mathbf{H}_m, \qquad \mathbf{R}_{k(jj)} = \sum_{l \in N_j} \sum_{m \in M_k} u_{lm}^q.$$

   Truncate u_{jk} to the range of $[0, 1]$ if necessary.

3. Compute class centroids using Eq.(4):

$$v_{mk} = \frac{(\mathbf{H}_m \mathbf{u}_k)^T \mathbf{W}_m (\mathbf{H}_m \mathbf{u}_k)}{||\mathbf{H}_m \mathbf{u}_k||^2}, \tag{4}$$

   for all $m = 1...M$ and $k = 1...K$, where

$$\mathbf{W}_{m(jj)} = y_{mj}.$$

4. Compute gain field by solving the following spatially varying difference equation for g_j:

$$\sum_{m=1}^{M} \sum_{k=1}^{K} (\mathbf{H}_m \mathbf{u}_k)_j^2 < \mathbf{y}_j, \mathbf{v}_k >= g_j \sum_{m=1}^{M} \sum_{k=1}^{K} (\mathbf{H}_m \mathbf{u}_k)_j^2 < \mathbf{v}_k, \mathbf{v}_k > + \lambda_1 (H_1 * g)_j + \lambda_2 (H_2 * g)_j. \tag{5}$$

   Here the convolution kernels H_1 and H_2 are given by:

$$\begin{aligned} H_1 &= \sum_{r=1}^{R} (D_r * \breve{D}_r)_j \\ H_2 &= \sum_{r=1}^{R} \sum_{s=1}^{R} \Big((D_r * D_s) * (\breve{D}_r * \breve{D}_s) \Big)_j \end{aligned}$$

   where $\breve{D}$ is the mirror reflection of the finite difference operator D(details can be found in [8]).

5. If the algorithm has converged, then exit; otherwise go to step 2.

In Eq.(3), when $\mathbf{C}_{k(ij)} = 0$ for all $i \neq j$ (i.e. all channels have an impulse point spread function), it reduces to the membership updating equation in FANTASM.[7] Due to the constraint that the membership functions must be between zero and one, truncation is applied when needed, which also helps to improve the stability of the algorithm. Eq.(5) can be solved efficiently using a multigrid algorithm .[8] The segmentation algorithm is

	Group1 1.6mm-ST 2.8 noise-STD	Group2 1.6mm-ST 5.6 noise-STD	Group3 3.0mm-ST 2.8 noise-STD	Group4 3.0mm-ST 5.6 noise-STD
Scan1	3.74	4.95	8.79	10.05
Scan2	3.63	4.84	8.17	9.23
Multi-channel FANTASM	2.75	3.45	6.55	7.16
New method	2.37	3.33	5.57	6.59

Table 1. Misclassification rate (in percentage)

considered to be converged when the maximum change in the membership values is less than a threshold (0.01 is used in this work).

We note that an extra registration step is necessary to properly align the multiple scans acquired at separate times before they can be used in the above algorithm. In this work, we use the AIR (automated image registration) software package developed by Woods et al.[10] for the registration of the original scans. We first use AIR to compute a rigid transformation between the two scans, and then use Cubic B-spline interpolation to transform both low-resolution scans to the same coordinate system. The images are resampled to have isotropic voxels the same size as that of the high-resolution image to be reconstructed.

3. RESULTS

We conducted several experiments using both simulated and real brain image data sets in order to test the performance of the proposed method. Skull-stripping was performed as a preprocessing step for all the experiments. The total number of tissue classes, K, was set to three, corresponding to white matter(WM), gray matter(GM) and cerebrospinal fluid(CSF).

In the first experiment, we used a high-resolution brain phantom image of size $256 \times 256 \times 256$ and an isotropic voxel size of $1 \times 1 \times 1\text{mm}^3$. We then simulated four groups of orthogonal low resolution (in slice-selection direction only) scans with varying slice thicknesses and signal-to-noise ratios. We performed a tissue segmentation using both the previous FANTASM method and our new algorithm and compared their accuracy by computing the misclassification rate, defined as the ratio of misclassified voxels to the total number of voxels within the brain volume. The FANTASM method was not only run on each individual scan separately, but also run using both scans in a multichannel mode as well. The results are summarized in Table 1, where Groups 1 and 2 have a slice thickness(ST) of 1.6 mm, and Groups 3 and 4 are 3.0 mm. The added white Gaussian noise in Groups 1 and 3 has a standard deviation(STD) of 2.8, while the noise level in Groups 2 and 4 is 5.6. From the results, it can be seen that the improvements using our new method increases as the anisotropy of the scans increase.

For visual comparison, we show in Fig. 1 the segmentation results (both fuzzy GM segmentation and hard brain segmentation) using the simulated data in Group 4 above.

One coronal slice of the truth image and also the simulated axial and coronal scans is shown in the first row of Figure 1 (left to right: truth, axial, and coronal). In this cross-section, the blurring of the axial scan is clearly seen along the vertical direction.

The fuzzy GM segmentation and the hard segmentation generated by the FANTASM method for the corresponding images are shown in rows 2 and 3 respectively. Again, in this cross-section, the error in the segmentation is more clearly seen for the simulated axial data.

Rows 4 and 5 show the fuzzy and the hard segmentation when using both low-resolution scans. In the left column, we applied FANTASM to a simple average of both scans after they are interpolated to isotropic voxel size as the truth. In the middle column, the two interpolated scans are used as two channels for a two-channel FANTASM segmentation. Interestingly, using the two scans in a multi-channel fashion gives much better segmentation accuracy than simply using their average. The best results are achieved by the new proposed method, as shown in the right column of the last two rows. We reach the conclusion that by incorporating the modeling of PSF, we can make better use of the resolution information in the low-resolution data.

In the second experiment, we use simulated multi-modality MR brain images obtained from the Brainweb simulated brain database.[11] In particular, we acquired two brain images simulated with T1-weighted and PD-weighted contrast respectively, and both having 1-mm cubic voxels, 0% noise, and 20% image intensity inhomogeneity. We then simulated two orthogonal low resolution images from the acquired images (both having slice thickness 2.0) and added 3% Gaussian noise. Fig. 2 shows the brain tissue segmentation results on the simulated data. One can see that the result of our method (f) best resembles the truth segmentation and it shows most clear anatomical details (indicated by arrows). We also computed the misclassfication error as in the first experiment, and the error rates are 6.57% for the T1-weighted image, 8.60% for the PD-weighted image, 5.53% for the result of two-channel FANTASM, and 5.29% for the result of our method.

In the experiment using real MR images, we used a randomly selected pair of T1-weighted axial and coronal scans from our database. Both scans have an in-plane resolution of $0.9375\text{mm} \times 0.9375\text{mm}$, and the slice-thickness is 1.5 mm and 1.6 mm, respectively. Due to the lack of an underlying truth model, we can only compare the results visually. Fig. 3 shows the hard-segmentation results derived from the fuzzy membership functions from different methods (the second row shows the magnified view). As can be seen, the new method better captures the thin strand of CSF within tight sulcal folds, which are often obscured by the partial volume averaging effect due to limited image resolution. The improvement can be expected to be more obvious when the individual scans have large anisotropicity in voxel size.

Although Fig. 3 demonstrates improvement in most part of the image, we have observed some degradation in the area close to the top of the brain image in both Fig. 3(c) and (d), where WM erroneously protrudes into the GM and CSF region. This degradation is caused by a susceptibility artifact existing only in the coronal scan, where an abrupt brightness variation is observed within that region. Because of the smoothness assumption made in Section 2.1, this artifact can not be modeled by the gain field, and thus can not be corrected by the segmentation algorithm. One approach to solving this problem would be to manually delineate the artifact region, and then use only the axial scan in this region for segmentation.

Using this data, we also compared the execution times of our algorithm against running the super-resolution reconstruction and segmentation algorithms separately. Our proposed algorithm required 330 seconds, while the two separate steps requires 585 seconds in sum.

4. CONCLUSIONS AND FUTURE WORK

We have developed a new multi-channel segmentation method that incorporates the point spread function of the imaging system. The current simulation and real data experiments show that the new algorithm achieves better segmentation resolution and accuracy. Additional validation studies using real multi-modality data and further research on the compensation of the susceptibility artifact are required. Future work also includes incorporation of edge-preserving regularization techniques.

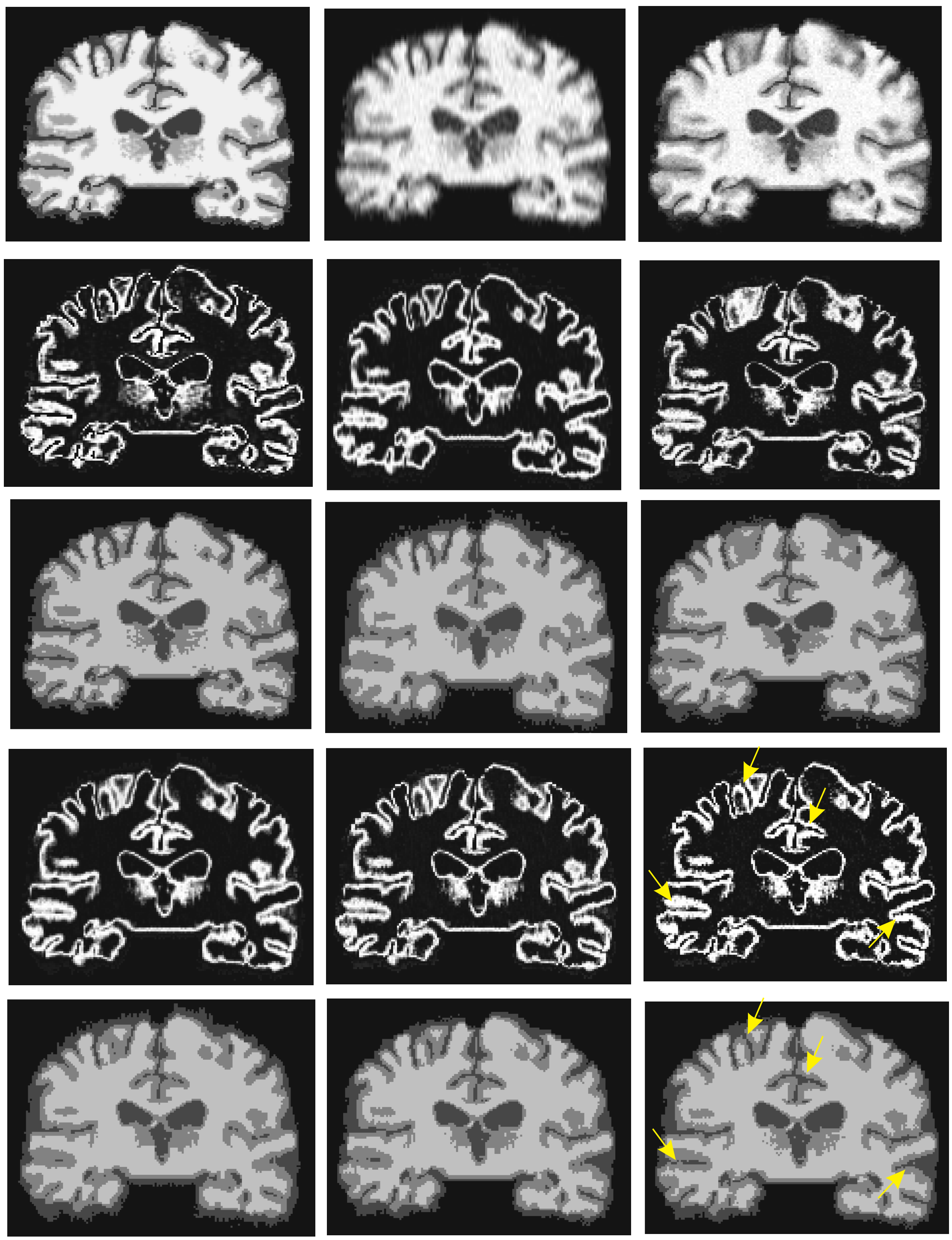

Figure 1. Brain tissue segmentation results on simulated data: The first row shows coronal cross-sections of (from left to right): the truth, the axial, and the coronal data. The second and the third rows show the fuzzy GM and the hard segmentations respectively, generated by applying FANTASM on each individual volume in the first row. The fourth and the fifth rows show the fuzzy and the hard segmentations using both low-resolution scans (axial and coronal): the left column is the result of running FANTASM on the average of the two scans; the middle column is the result of a two-channel FANTASM; the right column is the result of the proposed method.

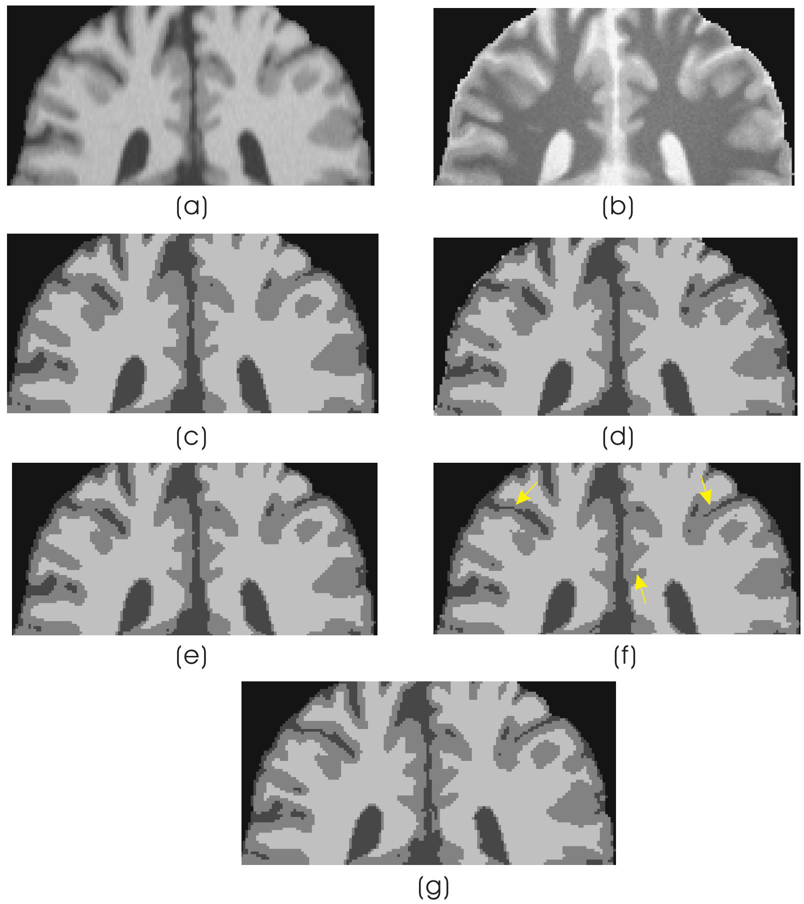

Figure 2. Brain tissue segmentation results on simulated multi-modality data (magnified view of a coronal cross-section): (a) the T1-weighted image; (b) the PD-weighted image; (c) hard-segmentation of FANTASM on the T1-weighted image; (d) hard-segmentation of FANTASM on the PD-weighted image; (e) hard-segmentation of a two-channel FANTASM using both images; (f) hard-segmentation of the new method using both images; (g) the truth model.

ACKNOWLEDGMENTS

We thank Dr. Susan Resnick for her guidance in using the BLSA data. This work is supported by NIH/NINDS grant 5 R01 NS037747.

REFERENCES

1. S. M. Resnick, A. F. Goldszal, C. Davatzikos, S. Golski, M. A. Kraut, E. J. Metter, R. N. Bryan, and A. B. Zonderman, "One-year age changes in MRI brain volumes in older adults," *Cerebral Cortex* **10**(5), pp. 464–472, 2000.
2. X. Han, D. L. Pham, D. Tosun, M. Rettmann, C. Xu, and J. L. Prince, "CRUISE: Cortical reconstruction using implicit surface evolution," *NeuroImage* **23**, pp. 997–1012, 2004.
3. Y. Bai, X. Han, and D. L. Prince, "Super-resolution reconstruction of mr brain images," in *38th Annual Conference on Information Sciences and Systems*, pp. I:1358–1363, 2004.
4. J. G. Tamez-Pena, S. Totterman, and K. J. Parker, "MRI isotropic resolution reconstruction from two orthogonal scans," in *Proceedings of SPIE*, **4322**, pp. 87 – 97, 2001.

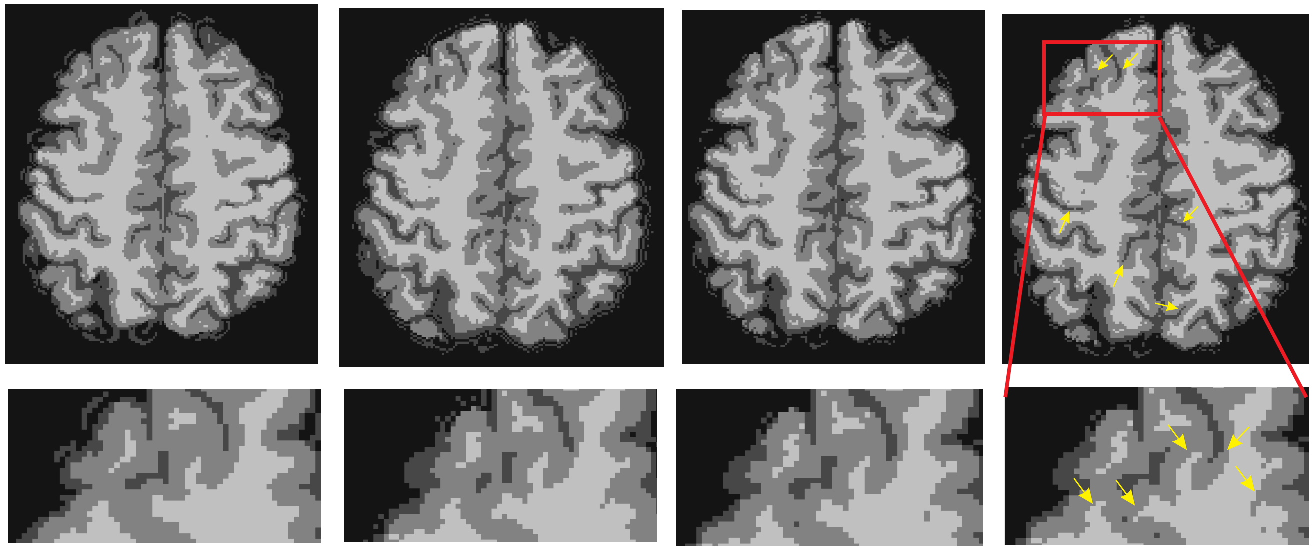

(a) (b) (c) (d)

Figure 3. Brain tissue segmentation results on real data: (a) using axial data only (b) using coronal data only (c) using multi-channel FANTASM (d) using our method. (Arrow-pointed region shows clear improvements.)

5. H. Greenspan, G. Oz, N. Kiryati, and S. Peled, "MRI inter-slice reconstruction using super-resolution," *Magnetic Resonance Imaging* **20**, pp. 437–446, 2002.
6. E. Roullot, A. Herment, I. Bloch, A. de Cesare, M. Nikolova, and E. Mousseaux, "Modeling anisotopic undersampling of magnetic resonance angiographies and reconstruction of a high-resolution isotropic volume using half-quadratic regularization techniques," *Signal Processing* **84**, pp. 743–762, 2004.
7. D. L. Pham, "Robust fuzzy segmentation of magnetic resonance images," in *The Fourteenth IEEE Symposium on Computer-Based Medical Systems(CBMS)*, **2001**, pp. 127–131, 2001.
8. D. L. Pham and J. L. Prince, "Adaptive fuzzy segmentation of magnetic resonance images," *IEEE Transactions on Medical Imaging* **18**, pp. 737–752, 1999.
9. J. L. Prince, Q. Tan, and D. L. Pham, "Optimization of mr pulse sequences for bayesian image segmentation," *Medical Physics* **22**, pp. 1651–1656, 1995.
10. R. P. Woods, S. T. Grafton, C. J. Holmes, S. R. Cherry, and J. C. Mazziotta, "Automated image registration: I. general methods and intrasubject, intramodality validation," *Journal of Computer Assisted Tomography* **22**, pp. 139–152, 1998.
11. R. K.-S. Kwan, A. C. Evans, and G. B. Pike, "MRI simulation-based evaluation of image-processing and classification methods," *IEEE Transactions on Medical Imaging* **18**(11), pp. 1085–1097, 1999.

APPENDIX A. DERIVATION OF ALGORITHM EQUATIONS

In this section, we derive the equations in the algorithm proposed in Section 2.2. To derive Eq.(3), we first rewrite the objective function (2) using a Lagrange multiplier κ_j to enforce the constraint that $\sum_{k=1}^{K} u_{jk} = 1$. Ignoring the unrelated regularization terms for the gain field, we get

$$J_{\text{new}}^{\lambda} \quad = \quad \sum_{m=1}^{M} \left(\frac{1}{\sigma_m^2} \sum_{k=1}^{K} (\mathbf{H}_m \mathbf{u}_k)^T \mathbf{B}_{mk} (\mathbf{H}_m \mathbf{u}_k) \right) + \frac{\beta}{2} \sum_{k}^{K} \mathbf{u}_k^T \mathbf{R}_k \mathbf{u}_k + \sum_j \kappa_j \left(\sum_{k}^{K} u_{kj} - 1 \right)$$

Taking the partial derivative with respect to u_{jk}, and setting the result equal to zero yields

$$\sum_{m=1}^{M} \frac{1}{\sigma_m^2} \left[\mathbf{H}_m^T \mathbf{B}_{mk} \mathbf{H}_m \mathbf{u}_k \right]_j + \beta (\mathbf{R}_k u_k)_j - \kappa_j = 0$$

Let $\mathbf{C}_k = \sum_m \frac{1}{\sigma_m^2} \mathbf{H}_m^T \mathbf{B}_{mk} \mathbf{H}_m$, Eq.(6) yields

$$u_{kj} = \frac{\kappa_j - \sum_{i \neq j} \mathbf{C}_{k(ji)} u_{ki}}{\mathbf{C}_{k(jj)} + \beta \mathbf{R}_{k(ji)}}$$

Substituting u_{jk} into the constraint equation on the membership functions results in

$$\kappa_j = \frac{1 + \sum_k \frac{\sum_{i \neq j} \mathbf{C}_{k(ji)} u_{ki}}{\mathbf{C}_{k(jj)} + \beta \mathbf{R}_{k(ji)}}}{\sum_k \frac{1}{\mathbf{C}_{k(jj)} + \beta \mathbf{R}_{k(ji)}}}$$

Substituting the value of κ_j back into Eq.(6), and rearranging yields Eq.(3).

The derivation of Eq.(4) and Eq.(5) are straightforward extensions of the corresponding equations in .[7]